hydrogen

MDPI

Article

Hydrogen-Powered Annular Combustor Design and Aerothermal Optimization for a Short-Haul Large-Bypass Turbofan Engine

Yash Chougale, Hossein Sheykhpoor and Hamidreza Gohari Darabkhani *

Department of Engineering, School of Digital, Technologies, Innovation and Business (DTIB), University of Staffordshire, Stoke-on-Trent ST4 2DE, UK; yash.chougale1@staffs.ac.uk (Y.C.)
* Correspondence: h.g.darabkhani@staffs.ac.uk

Abstract

Commercial aviation contributes approximately 3% of global CO_2 emissions, while nitrogen oxides (NO_x) remain a major environmental concern. Hydrogen is a promising carbon-free fuel for future gas turbine engines and offers a potential pathway towards net-zero aviation. This study presents the aerothermal design and CFD-based iterative refinement of an annular combustor for a hydrogen-fuelled CFM56-class large-bypass turbofan. The combustor was initially sized using established design correlations, with GasTurb14 providing the engine-cycle boundary conditions. CFD simulations were performed to evaluate the airflow distribution, temperature field, pressure loss and NO_x formation, and to optimize the cooling-hole arrangement. The final combustor achieved the target exit temperature of 1500 K with a pressure loss of 5.9%, meeting the design objective of approximately 6%. Relative to the initial hydrogen-fuelled configuration, the redesigned cooling-hole layout reduced the fuel-to-air ratio required to achieve the target exit temperature from 0.009 to 0.0073 (18.9%) and reduced the exit NO mass fraction from 0.003443 to 0.002223. A separate Large Eddy Simulation (LES) of the final combustor geometry was conducted to compare the combustion characteristics of hydrogen and Jet-A under identical operating conditions. The results demonstrate that cooling-hole configuration has a significant influence on combustor thermal performance and NO_x emissions, providing design guidance for future hydrogen-fuelled gas turbine combustors. Owing to the absence of experimental data for this configuration, the results are presented as a computational design study supported by a benchmark comparison rather than as an experimental validation.

Keywords: hydrogen; turbofan engine; combustor design; low NO_x

1. Introduction

The aviation industry plays a crucial role in the global economy, supporting nearly 90 million jobs and contributing over 4% of the worldwide GDP [1]. However, this sector is also a significant contributor to greenhouse gas emissions, accounting for approximately 3% of global CO_2 emissions [2]. As the urgency to address climate change intensifies, the aviation industry faces increasing pressure to reduce its carbon footprint and align with international climate targets, particularly the ambitious goal of achieving net-zero emissions by 2050 [3]. To meet this target, the sector is exploring various strategies, including the adoption of sustainable aviation fuels (SAFs), advances in propulsion technology, and improvements in air traffic management [4]. In this context, the present project focuses on developing a hydrogen-powered turbofan engine with an annular combustion chamber,

Academic Editor: Guo-Ming Weng

Received: 30 June 2026
Revised: 1 August 2026
Accepted: 5 August 2026
Published: 20 August 2026

targeting the short-haul commercial aviation segment. This focus is relevant because short-haul flights account for a large proportion of commercial flight movements [5]. The project aims to significantly reduce emissions in this high-impact segment by optimizing engine designs similar to the widely used CFM56 engine. The CFM56 serves as a reference point due to its prevalence in short-haul fleets, allowing for an efficient transition to hydrogen while leveraging existing infrastructure.

Hydrogen can be produced through several established pathways, including steam methane reforming (SMR), coal gasification, biomass conversion, methane pyrolysis, and water electrolysis. At present, over 95% of global hydrogen production is derived from fossil-fuel-based processes, primarily SMR, owing to its technological maturity and relatively low production cost. However, these conventional production routes are associated with significant carbon dioxide emissions, limiting their long-term sustainability despite the implementation of carbon capture and storage technologies [6,7]. Consequently, considerable research efforts have focused on the development of low-carbon hydrogen production technologies capable of supporting global decarbonization targets.

Among the available production pathways, water electrolysis powered by renewable electricity is widely recognised as the most promising route for producing green hydrogen with minimal lifecycle greenhouse gas emissions [7,8]. Current electrolysis technologies include alkaline water electrolysis (AWE), proton exchange membrane electrolysis (PEM), solid oxide electrolysis (SOEC), and anion exchange membrane electrolysis (AEM), each offering distinct advantages regarding efficiency, operating temperature, dynamic response, technological maturity, and scalability [7,8]. As renewable electricity generation continues to expand and electrolyser technologies improve, green hydrogen is expected to become increasingly cost-competitive, enabling its large-scale deployment across difficult-to-decarbonise sectors such as aviation, heavy transportation, steel manufacturing, and power generation [6,9]. Nevertheless, challenges related to production costs, storage, transportation, and hydrogen infrastructure remain significant barriers to widespread adoption, highlighting the need for continued technological innovation and system-level optimization [7,9].

Alternative aviation fuels include SAFs, hydrogen, ammonia, and e-fuels. SAFs, derived from renewable biomass and waste, can reduce U.S. transportation emissions by 9–12% [10–12]. However, they are not fully carbon-neutral, especially if carbon is sourced from industrial processes rather than directly from the atmosphere [13]. Hydrogen, in contrast, offers 2.8 times more energy per kilogram than kerosene and emits only water vapor, eliminating carbon emissions entirely [14]. At fleet level, accelerated adoption of hydrogen-powered aircraft could reduce aviation's climate impact by approximately 60% in 2050 compared with an SAF-based baseline, although the magnitude of the benefit depends strongly on the assumptions applied to contrail effects [15]. However, hydrogen combustion presents unique challenges due to its high flame speed, and increased tendency for thermal NO_x formation compared to conventional aviation fuels [16,17]. Additionally, hydrogen's low volumetric density requires 4–5 times more storage volume, necessitating the use of cryogenic tanks and advanced insulation systems [18,19]. These storage constraints demand significant modifications to aircraft design, thus emphasizing the importance of optimizing the engine configuration to accommodate hydrogen. Unlike SAFs, which may not achieve full carbon neutrality, hydrogen inherently avoids the challenges of carbon-based emissions, positioning it as a superior alternative for sustainable aviation [20].

The annular combustion chamber has been selected for this project due to its superior performance characteristics, particularly when using hydrogen. As highlighted by El Sayed (2017) [21], the annular design offers streamlined aerodynamics, reducing drag and optimizing fuel efficiency. This design is especially advantageous given hydrogen's unique thermo-transport properties, which require efficient combustion dynamics. The compact and space-efficient nature of the annular chamber allows it to integrate seamlessly into existing aircraft designs without substantially increasing engine size or weight, which is critical for accommodating hydrogen's larger storage requirements. Additionally, the annular combustor experiences lower pressure losses than tubular or can-type designs, enhancing overall engine performance and reducing fuel consumption. Furthermore, the annular configuration supports uniform airflow distribution and stable combustion, which are essential for hydrogen's high flame speed and low ignition energy [22,23]. By leveraging the benefits of the annular combustor design, this project aims to maximize the performance and efficiency of a hydrogen-powered turbofan engine, thereby contributing to the aviation industry's sustainability goals. The transition to hydrogen-fueled gas turbines is a key step toward achieving net-zero aviation, driven by the need to reduce CO_2 emissions from conventional jet fuels. However, hydrogen combustion presents unique challenges in annular combustors, particularly in aerospace applications. While industrial hydrogen combustors have been studied [24–26], their operational conditions differ significantly from aviation gas turbines, which must operate efficiently at high altitudes and varying duty cycles.

Several studies have explored hydrogen combustion in annular combustors, either as a blended fuel with natural gas or as pure hydrogen. Moëll et al. (2018) [24] conducted Large Eddy Simulations (LESs) on hydrogen-enriched methane–air combustion in an industrial gas turbine burner, highlighting the significant impact of pressure on flame stability and NO_x formation. Similarly, Hernandez et al. (2021) [25] investigated the use of hydrogen in full-scale annular combustors, emphasizing the need for optimized fuel–air mixing strategies to control combustion instabilities. More recently, Cerutti et al. (2023) [26] developed a full-scale hydrogen combustor, focusing on flashback resistance, NO_x emissions, and injector design, confirming that hydrogen requires modified injection and cooling strategies compared to Jet-A. While these studies provide valuable insights into hydrogen combustion dynamics, they primarily focus on ground-level conditions or industrial applications. In contrast, aviation gas turbines operate under significantly different thermodynamic conditions at high altitudes, where the reduced air mass flow leads to increased fuel flow rates, resulting in higher flame temperatures and increased thermal NO_x formation. To mitigate these effects, a well-optimized aerothermal design is essential for hydrogen combustors in aircraft engines. Moëll et al. (2018) [24] also showed that at high pressures, the laminar flame speed of hydrogen decreases due to changes in reaction kinetics, while the turbulent flame speed increases, causing the flame to stabilize further upstream. This flame behavior makes combustor cooling even more critical in aviation applications.

Domingues et al. (2022) [27] investigated the feasibility of hydrogen combustion in the CFM56 engine, evaluating its performance under different duty cycles using boundary conditions from the ICAO database. However, the ICAO database lacks hydrogen-specific experimental data for large bypass aero-engines at high altitudes, leading to potential uncertainties in boundary conditions accuracy. Additionally, Domingues et al. (2022) [27] observed that hydrogen combustion resulted in higher liner wall temperatures than Jet-A, indicating the need for optimized cooling hole configurations. Their study was based on standard benchmark conditions, which do not necessarily reflect the best performance settings for hydrogen combustion. Their research utilized boundary conditions from the ICAO emissions database to evaluate performance metrics, including NO_x emissions and combustor efficiency. The study primarily examined hydrogen combustion at various power settings and compared its characteristics with conventional jet fuels. This study develops an optimized cooling system and boundary conditions for a hydrogen-fueled annular combustor operating at cruise altitude (10 km). GasTurb14 software is used to generate boundary conditions that better represent real engine operating conditions for hydrogen combustion in aerospace applications. High pressures cause the flame to stabilize further upstream, increasing NO_x emissions, as observed by Moëll et al. (2018) [24]. To address these effects, this study optimizes cooling hole distribution and diameter to achieve improved thermal uniformity and lower peak temperatures. Previous research has primarily examined hydrogen combustion at ground-level conditions, whereas this study investigates the impact of optimized cooling strategies and boundary conditions on hydrogen combustion in high-altitude cruise conditions.

The present study extends the work of Domingues et al. (2022) [27] through three distinct contributions. First, unlike the previous study, which adopted landing-and-take-off boundary conditions from the ICAO emissions databank, the present work derives the combustor inlet conditions from a GasTurb14 cycle model of a CFM56-class turbofan operating at representative engine conditions. The complete engine-cycle input set is provided in Table 1, ensuring that the operating conditions are fully reproducible. Second, the combustor cooling architecture is redesigned by replacing the benchmark stacked-ring cooling arrangement with a zone-specific configuration comprising a larger number of smaller cooling holes inclined at $\pm 45^\circ$. The influence of the redesigned cooling layout on the combustor thermal field and NO_x formation is evaluated independently under identical operating conditions, allowing the geometric effects to be isolated from those of the engine operating point. Third, the study extends beyond steady-state design analysis by performing a Large Eddy Simulation (LES) of the final combustor geometry using both hydrogen and Jet-A fuels. Together, these contributions provide a more comprehensive assessment of hydrogen combustor aerothermal performance and cooling design than previously reported.

Table 1. GasTurb14 cycle model inputs and combustor-relevant outputs.

Parameter	Sea-Level Static Design Point	CFD Operating Condition	Unit
Overall Pressure Ratio (OPR)	35.7	35.7	—
Fan Pressure Ratio	1.83	1.48	—
Combustor Inlet Total Temperature, T_3	915.96	800	K
Combustor Exit Temperature (T_4)	1800	1500	K
Combustor Inlet Total Pressure, P_3	3.65	3.4	MPa
Combustor Outlet Total Pressure, P_4	3.46	3.2	MPa
Combustor Pressure Drop	5.2	5.9	%
Air Mass Flow (Full Annulus)	110.9	110	kg/s
Hydrogen Fuel Mass Flow (Full Annulus)	1.12	0.9	kg/s
Altitude	0	10,000	m
Combustor Efficiency (assumed)	99	99	%

To achieve the project's goal of designing a hydrogen-powered gas turbine engine with an annular combustion chamber, several parameters and conditions were defined based on a comprehensive literature review and project requirements. Essential reference data—such as temperatures, pressure, velocity, and mass flows—were gathered using GasTurb version 14 software, calibrated for cruising aircraft conditions, to ensure realistic simulation inputs. The methodology for designing the combustor, as outlined by Melconian and Modak (1985) [28], serves as the core framework for calculating the fundamental dimensions of the annular combustion chamber. The detailed methodologies and essential formulas for calculating the fundamental dimensions of an annular combustion chamber were drawn from Lefebvre & Ballal (2010), Mark & Selwyn (2016), and Dharmalingam & Kothari (2021) [29–31].

https://doi.org/10.3390/hydrogen7030121

2. Methodology

2.1. Overall Workflow and Software Chain

The methodology follows a five-stage workflow, beginning with engine cycle analysis and concluding with unsteady combustion simulations. The overall process is summarised below.

(i) Cycle analysis. A two-spool, separate-exhaust turbofan representative of the CFM56 class is modelled in GasTurb14 to determine the combustor inlet total temperature, total pressure, air mass flow rate, and fuel mass flow rate at the selected operating condition. The complete engine-cycle inputs and the resulting combustor boundary conditions are presented in Table 1.

(ii) Preliminary combustor sizing. The combustor reference area, liner and casing dimensions, diffuser geometry, swirler configuration, and zonal air distribution are determined using established gas turbine combustor design correlations. These calculations provide the baseline combustor geometry for the subsequent CFD analysis.

(iii) Geometry generation. The combustor is modelled as a three-dimensional solid in SolidWorks and exported to ANSYS SpaceClaim version 2023 R2, where the fluid domain is extracted, simplified, and reduced to the periodic sector used for the CFD simulations.

(iv) Mesh generation and CFD setup. The fluid domain is discretised in ANSYS Meshing using an unstructured tetrahedral mesh. Steady reacting-flow simulations are performed in ANSYS Fluent 2023 R2 using the non-premixed RANS formulation described in Section 2.6. The flamelet library is generated within Fluent prior to the flow solution using the selected hydrogen reaction mechanism and is subsequently accessed during the CFD calculations to evaluate the combustion chemistry.

(v) Design refinement and unsteady analysis. The cooling-hole configuration is iteratively refined through successive CFD simulations to improve combustor performance. After the final geometry is established, a Large Eddy Simulation (LES) is performed to investigate the transient combustion behaviour of both hydrogen and Jet-A fuels.

The preliminary combustor dimensions are obtained from established design correlations, while the cooling-hole configuration is refined through iterative CFD-guided engineering judgement rather than a formal optimization algorithm. This approach provides a practical framework for evaluating the influence of combustor geometry on aerodynamic, thermal, and emissions performance.

2.2. Cycle Conditions and CFD Boundary Conditions

The combustor boundary conditions were obtained from a GasTurb14 model of a two-spool, separate-exhaust turbofan representative of the CFM56 class. The preliminary combustor sizing was performed using the sea-level static design point, while all CFD simulations were conducted at the operating condition listed in Table 1. The operating conditions reported correspond to the combustor inlet and outlet conditions required for the CFD simulations. Unless otherwise stated, all pressures are reported as absolute values.

The combustor design methodology followed the approach of Melconian and Modak (1985) [28] to determine critical design parameters, with reference conditions extracted from GasTurb14 software at a cruising thrust of 80% to simulate realistic operational conditions. The combustor outlet temperature was limited to 1673.15 K to minimize NO_x emissions, aligning with the recommendations of Hodzic and Kazagic (2018) [32] for environmentally compliant designs. Table 2 gives the reference values used.

Table 2. Reference Values.

Parameter	Value	Unit
Velocity (V)	118.50	m/s
Gas Constant (R)	286.90	J/kg·K
T_{max}	1673.15	K
Air mass flow rate ($\dot{m}_3$)	110.90	kg/s
T_3	915.96	K
P_3	3.65	MPa
T_4	1473.15	K
P_4	3.46	MPa

Lefebvre and Ballal (2010) [29] provided key considerations for the combustor pressure loss, combustor pressure drop factor, and liner pressure drop factor to calculate the reference area, which are as follows: $(\Delta P_{3\text{-}4}/P_3) = 0.06$, $(\Delta P_{3\text{-}4}/q_{ref}) = 20$ and $(\dot{m}_3 \cdot T_3^{0.5}/A_{ref} \cdot P_3) = 0.0046$. These considerations were applied to calculate the reference area, using Equation (1):

$$A_{ref} = [(R/2) \cdot (\dot{m}_3 \cdot T_3^{0.5}/P_3)^2 \cdot (\Delta P_{3\text{-}4}/q_{ref}) \cdot (\Delta P_{3\text{-}4}/P_3)^{-1}]^{0.5} = 0.201\ m^2 \quad (1)$$

According to Fear (1973) [33], the internal casing diameter was assumed to be 0.5 m, and the liner and reference diameters were calculated from the annular area, ensuring that air distribution and flow characteristics matched annular combustor configurations. A diffuser angle of 29° was incorporated to optimize flow recovery while minimizing pressure losses. The swirler design used a 3% pressure drop across the component with a swirl constant of 1.3, and a hub-to-swirler diameter ratio of 0.5 to achieve a recirculation zone angle of approximately 38°.

2.3. Air Distribution and Cooling-Hole Design

The air distribution methodology was guided by Darabkhani et al. (2022) [34], allocating 20% of the oxidant flow to the swirlers and dome cooling, with the remaining 80% distributed among the primary, secondary, and dilution zones. Table 3 gives the percentage of mass flow rate through each section with respective mass flow.

Table 3. Air Flow Distribution.

Components	Mass Flow (%)	Mass Flow Rate (kg/s)
Inlet	100%	110.9
Snout	20%	22.18
Swirler	12%	13.308
Dome Cooling	8%	8.872
Annulus	80%	88.72
Primary Zone	20%	22.18
Secondary Zone	10%	11.09
Dilution Zone	10%	11.09
Cooling Holes	40%	44.36

The regulation of airflow within the liner is managed through strategically positioned openings, which can be either plain or designed as 'stacked ring' cooling holes. The design process for these openings follows a systematic, iterative approach as outlined by Darabkhani (2022) [34]. In this study, the airflow opening design is modeled after the larger combustion chamber of the CFM56 engine [27]. The adopted pattern divides both the primary zone (PZ) and secondary zone (SZ) into two segments each, while the dilution zone (DZ) is segmented into three parts. To optimize the cooling hole configuration, two approaches were evaluated:

1. **Initial Approach (Without Cooling Holes):** This configuration establishes the airflow behavior of the baseline geometry at reduced computational cost and provides the reference against which the effect of the wall cooling patterns is assessed. Because no wall cooling holes are present, the 40% of inlet air allocated to them in Table 3 is redistributed among the primary, secondary and dilution zones. The percentage column in Table 4 is therefore the split within each zone after that redistribution, not a fraction of the total inlet flow.

Table 4. Hole Diameters and Air Mass Flow Rates in Respective Zones for Initial Approach.

Zone	Number of Holes	Mass Flow Respective with Table 3 (%)	Mass Flow Rate (kg/s)	d_h (mm)
PZ 1	40	50	16.6	19
PZ 2	40	50	16.6	19
SZ 1	40	50	11.1	15
SZ 2	40	50	11.1	15
DZ 1	50	33.33	7.39	11
DZ 2	50	33.33	7.39	11
DZ 3	50	33.34	7.39	11

2. **Final Approach (With Cooling Holes):** The number and diameter of the wall cooling holes were adjusted iteratively across successive simulations to obtain the required cooling without degrading combustion. In Table 5 the percentage column is the fraction of the total combustor inlet flow; the wall cooling holes carry a separate allocation given in Table 6.

Table 5. Hole Diameters and Air Mass Flow Rates in Respective Zones (with cooling holes) for Final Approach.

Zone	Number of Holes	Mass Flow Respective with Table 3 (%)	Mass Flow Rate (kg/s)	d_h (mm)
PZ 1	40	10	11.09	15.5
PZ 2	40	13	14.42	17.7
SZ 1	40	5	5.545	11
SZ 2	40	6	6.654	12
DZ 1	50	3.00	3.327	7.6
DZ 2	50	3.00	3.327	7.6
DZ 3	50	4.00	4.436	8.8

Table 6. Hole diameters and air mass flow rates for the wall cooling holes.

Zone	Number of Holes	Mass Flow Respective with Table 3 (%)	Mass Flow Rate (kg/s)	d_h (mm)
PZ	350	15	16.635	6.4
SZ	350	15	16.635	6.4
DZ	400	10	11.09	4.9

The benchmark wall-cooling configuration proposed by Darabkhani et al. [34] and Mark and Selwyn [30] were adopted as the initial design. CFD analysis showed that this configuration excessively cooled the primary combustion zone, resulting in a combustor exit temperature below the design target. Consequently, the cooling-hole arrangement was iteratively refined to achieve a more balanced distribution of cooling air while maintaining adequate liner protection.

A zone-specific cooling strategy, inspired by low-emission cooling concepts reported by Liu et al. [35], was investigated. Initial modifications involving larger cooling holes in regions of high thermal loading redistributed the hot spots but did not reduce their magnitude. The final configuration therefore employed a greater number of smaller cooling holes, producing a more uniform cooling distribution, reducing local peak near-wall gas temperatures, and improving the combustor exit temperature profile.

The air mass-flow distribution assigned to each combustor zone and the corresponding cooling-hole diameters are presented in Tables 4 and 5, respectively. The cooling-hole diameters were determined using Equations (2) and (3). In Equation (2), $\dot{m}_j$ represents the air mass flow rate through an individual cooling-hole row, n is the number of holes within that row, P_3 and T_3 are the combustor inlet total pressure and temperature, and P_L is the liner static pressure at the corresponding axial location. In Equation (3), the discharge coefficient, C_D, was assumed to be 0.6 for all cooling-hole rows. The final cooling-hole configuration is summarised in Table 6.

The cooling-hole arrangement was refined through an iterative CFD-guided engineering design process rather than a formal numerical optimisation. Each design iteration was assessed against three performance criteria: (i) achieving the target combustor exit temperature of 1500 K, (ii) reducing peak near-wall gas temperatures without introducing new local hot spots, and (iii) maintaining a combustor pressure loss of approximately 6%. The final configuration represents the first design that simultaneously satisfied all three criteria.

The initial combustor geometry was generated using established empirical design correlations to provide a physically consistent baseline for the CFD analysis. The primary objective of this study was to investigate the influence of cooling-hole configuration on combustor aerothermal performance and NO_x emissions rather than to develop a new combustor sizing methodology. Future work will consider automated optimisation techniques, including surrogate-assisted and gradient-based approaches, to further optimise cooling-hole diameter, number, location, and injection angle using multiple performance objectives.

$$\mathrm{d_j} = [(15.25 \cdot \dot{\mathrm{m}}_\mathrm{j} \cdot (\mathrm{P_3} \cdot \mathrm{P_L}/\mathrm{T_3})^{-0.5})^{1/2}]/\mathrm{n} \tag{2}$$

$$\mathrm{d_h} = \mathrm{d_j}/\mathrm{C_D}^{0.5} \tag{3}$$

2.4. Computational Domain, Sector Definition and Mass-Flow Scaling

Figure 1 illustrates the annular combustor geometry, which was created in SolidWorks version 2023 and has an overall length of 0.4 m. The full annulus consists of 20 equally spaced swirlers, giving a rotational periodicity of 18°. Consequently, a single 18° sector containing one swirler represents the smallest periodic computational domain.

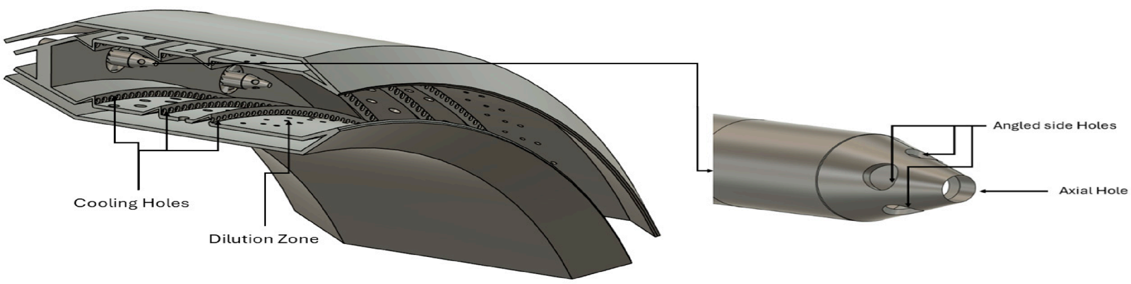

Figure 1. Schematic of the Hydrogen Combustor for the Turbofan Engine (54-Degree Section), with an Inset Showing a Detailed View of the Fuel Nozzle.

Two computational domains were employed in this study. All steady Reynolds-Averaged Navier–Stokes (RANS) simulations, including the baseline configuration, benchmark cooling layout, intermediate cooling-hole designs, and final cooling configuration, were performed using a single 18° periodic sector. Following completion of the design refinement, the final combustor geometry was re-meshed as a 54° sector containing three swirlers for the Large Eddy Simulation (LES). The larger computational domain allows the development of azimuthal flow structures extending across multiple swirler passages, which cannot be captured using a single-passage periodic domain.

The combustor incorporates 45° vane-angle swirlers and a hydrogen fuel injector comprising one central axial injection hole and four inclined side holes. The axial passage delivers fuel directly into the primary combustion zone, while the inclined side holes enhance fuel–air mixing by promoting swirling motion and improving fuel dispersion within the combustor.

The inlet mass flow rates applied to each computational domain were scaled directly from the full-annulus values according to the sector angle. For the steady RANS simulations, the 18° sector represents one-twentieth of the full annulus, resulting in an inlet air mass flow rate of 5.50 kg/s and a hydrogen mass flow rate of 0.040 kg/s, corresponding to a fuel-to-air ratio of 0.0073. For the LESs, the 54° sector represents three-twentieths of the full annulus, giving inlet mass flow rates of 16.5 kg/s for air and 0.120 kg/s for hydrogen. The fuel-to-air ratio remains unchanged because both the air and fuel mass flow rates are scaled proportionally with the computational sector.

2.5. Combustion and Turbulence Modelling

The combustor simulations were performed using ANSYS Fluent 2023 R2 to investigate hydrogen combustion within the proposed gas turbine combustor. All cases were modelled using the non-premixed combustion model, providing a consistent combustion framework for both hydrogen and Jet-A while accommodating their markedly different chemical reactivities. Compared with lean-premixed combustion, the non-premixed formulation is less susceptible to flashback and flame instability when modelling highly reactive fuels such as hydrogen, making it suitable for comparative multi-fuel investigations [36].

Turbulence was modelled using the k–ω Shear Stress Transport (SST) model, which has demonstrated reliable performance in swirling and highly sheared combusting flows [37]. The governing equations for mass, momentum, energy, and species transport were solved using the pressure-based solver in Fluent. The Dufour effect, pressure work, viscous heating, surface reactions, and gas radiation were neglected [38].

The choice of a non-premixed combustion model represents a modelling trade-off rather than an assertion that it is the preferred combustion strategy for hydrogen-fuelled gas turbines. Hydrogen combustion in a non-premixed configuration produces reaction zones close to stoichiometric conditions, where flame temperatures are highest and thermal NO formation is consequently enhanced. Accordingly, the NO_x levels predicted in this study should be interpreted within the context of the selected combustion model. The primary objective of this work is to evaluate the influence of combustor cooling architecture under identical modelling assumptions, allowing meaningful comparisons between design iterations and between hydrogen and Jet-A using a consistent numerical framework.

Steady Reynolds-Averaged Navier–Stokes (RANS) simulations were employed for the combustor design and refinement because they provide a practical balance between computational cost and predictive capability during iterative engineering design. The final combustor configuration was subsequently investigated using Large Eddy Simulation (LES) to provide additional insight into the transient flow and combustion characteristics. Owing to the substantially higher computational cost of LES, the simulations were performed

https://doi.org/10.3390/hydrogen7030121

over a finite physical time using a time step of 1×10^{-6} s, representing a computationally feasible compromise for the available resources while resolving the dominant unsteady flow structures within the combustor.

$$\nabla \cdot (\rho u) = 0 \quad (4)$$

$$\rho(u \cdot \nabla u) = -\nabla p + \nabla \cdot (\mu(\nabla u + \nabla^t u)) - (2/3)\nabla \cdot uI \quad (5)$$

$$\nabla \cdot u(\rho E_f + p) = \nabla[k_{eff}\nabla T - \Sigma_j h_j J_j] + (\mu[\nabla u + (\nabla \cdot u)^T - (2/3)\nabla \cdot uI] \cdot u + S_f{}^h = 0 \quad (6)$$

where $\boldsymbol{u}$ is the variable for gas velocity, $\boldsymbol{p}$ for absolute pressure, and $\boldsymbol{T}$, $\boldsymbol{\rho}$, $\boldsymbol{\mu}$, $\boldsymbol{I}$, $\boldsymbol{k_{eff}}$, $\boldsymbol{E_f}$, $\boldsymbol{h_j}$, $\boldsymbol{J_j}$, $\boldsymbol{S_f{}^h}$ denote temperature, gas density, molecular viscosity, unit tensor, effective conductivity, total fluid energy, enthalpy, and diffusion flux of species j and the fluid source term, respectively.

Li et al.'s (2004) [39] hydrogen reaction mechanism was employed to generate the flamelet library used in the non-premixed combustion model. Although originally developed using experimental data over a range of operating conditions, the mechanism has also been evaluated for gas turbine hydrogen combustion and shown to provide satisfactory predictions under elevated-pressure conditions [40]. In the present study, it was selected to provide a consistent chemical kinetic framework for all simulations. As with any reduced or detailed chemical mechanism applied outside its original validation range, some uncertainty remains in the prediction of absolute quantities such as NO_x emissions. Consequently, the predicted NO_x values should be interpreted within the context of the selected reaction mechanism.

Thermal radiation was not included in the CFD simulations. Under hydrogen combustion, the high concentration of water vapour in the combustion products can increase radiative heat transfer to the combustor liner, potentially influencing both the gas temperature distribution and the liner thermal loading. Neglecting radiation may therefore affect the predicted absolute wall temperatures and NO_x formation. However, because the same modelling assumptions were applied consistently to every combustor configuration investigated, the simulations remain suitable for comparing the relative effects of different cooling-hole arrangements on combustor performance. Future work will incorporate participating-media radiation models to further improve the prediction of combustor thermal behaviour under hydrogen combustion.

$$\nabla \cdot (\rho u \cdot Y_j) = -\nabla J_j + R_j \quad (7)$$

Nitrogen oxide (NO_x) emissions were predicted using the methodology adopted by Domingues et al. [27]. For the hydrogen simulations, the Fluent NO_x model included only the thermal (extended Zeldovich) mechanism, as this is the dominant NO formation pathway under the non-premixed hydrogen combustion conditions considered in this study. The prompt (Fenimore) mechanism was not included because it depends on hydrocarbon radicals, which are absent in hydrogen combustion. For the Jet-A LESs, the prompt mechanism was enabled owing to its physical relevance. The NNH and N_2O-intermediate pathways were not considered. Although these mechanisms may contribute under lean, high-pressure hydrogen combustion, thermal NO formation remains the dominant pathway under the near-stoichiometric conditions of the present non-premixed flame. Consequently, the reported NO_x values should be interpreted within the limitations of the adopted modelling approach.

The combustion chemistry was represented using the steady flamelet model available in ANSYS Fluent. The flamelet library was generated internally from the Li et al. (2004) [39] hydrogen reaction mechanism shown in Table 7 and consisted of 32 diffusion flamelets discretised over 64 grid points. Thermodynamic properties were evaluated using the Peng–Robinson equation of state [41], while mixture properties were calculated using Fluent's mixing-law formulation.

Table 7. H_2/O_2 Combustion Mechanism.

			A (cm, mol, s)	*n*	E (kCal/mol)
1.	$H + O_2 \rightleftharpoons$	$O + OH$	3.55 × 1015	−0.41	16.6
2.	$O + H_2 \rightleftharpoons$	$H + OH$	5.08 × 104	2.67	6.29
3.	$H_2 + OH \rightleftharpoons$	$H_2O + H$	2.16 × 108	1.51	3.43
4.	$O + H_2O \rightleftharpoons$	$OH + OH$	2.97 × 106	2.02	13.4
5.	$H_2 + M \rightleftharpoons$	$H + H + M$ a	4.58 × 1019	−1.40	104.38
6.	$O + O + M \rightleftharpoons$	$O_2 + M$ a	6.16 × 1015	−0.5	0.00
7.	$O + H + M \rightleftharpoons$	$OH + M$ a	4.71 × 1018	−1.0	0.00
8.	$H + OH + M \rightleftharpoons$	$H_2O + M$ b	3.80 × 1022	−2.00	0.00
9.	$H + O_2 + M \rightleftharpoons$	$HO_2 + M$ c	6.37 × 1020	−1.72	0.52
10.	$HO_2 + H \rightleftharpoons$	$H_2 + O_2$	1.66 × 1013	0.00	0.82
11.	$HO_2 + H \rightleftharpoons$	$OH + OH$	7.08 × 1013	0.00	0.30
12.	$HO_2 + O \rightleftharpoons$	$OH + O_2$	3.25 × 1013	0.00	0.00
13.	$HO_2 + OH \rightleftharpoons$	$H_2O + O_2$	2.89 × 1013	0.00	−0.50
14.	$HO_2 + HO_2 \rightleftharpoons$	$HO_2 + O_2$ d	4.20 × 1014	0.00	11.98
	$HO_2 + HO_2 \rightleftharpoons$	$HO_2 + O_2$	1.30 × 1011	0.00	−1.63
15.	$H_2O_2 + M \rightleftharpoons$	$OH + OH + M$ e	1.20 × 1017	0.00	45.5
			2.94 × 1014	0.00	48.4
16.	$H_2O_2 + H \rightleftharpoons$	$H_2O + OH$	2.41 × 1013	0.00	3.97
17.	$H_2O_2 + H \rightleftharpoons$	$H_2 + HO_2$	4.82 × 1013	0.00	7.95
18.	$H_2O_2 + O \rightleftharpoons$	$OH + HO_2$	9.55 × 106	2.00	3.97
19.	$H_2O_2 + OH \rightleftharpoons$	$H_2O + HO_2$ d	1.00 × 1012	0.00	0.00
	$H_2O_2 + OH \rightleftharpoons$	$H_2O + HO_2$	5.80 × 1014	0.00	9.56

a. Efficiency factors are: εH_2O = 12.0, εH_2 = 2.5; b. Efficiency factors are: εH_2O = 12.0, εH_2 = 2.5; c. Troe parameter is Fc = 0.8. Efficiency factors are: εH_2O = 11.0, εH_2 = 2.0, and εO_2 = 0.78; d. reactions 14 and 19 are expressed as the sum of the two rate expressions; e. Troe parameter is Fc = 0.5. Efficiency factors are: εH_2O = 12.0, εH_2 = 2.5.

The NO mass fraction was obtained by solving a transport equation following convergence of the reacting-flow solution. In this approach, the NO field is calculated using the converged temperature, velocity, density, and species fields, with the reaction rates evaluated through Fluent's thermal NO_x model. Because the predicted NO concentrations are small, the NO field does not influence the combustion solution and is therefore treated as a passive scalar.

Steady Reynolds-Averaged Navier–Stokes (RANS) simulations coupled with the steady flamelet model were employed throughout the combustor design process to provide a computationally efficient framework for evaluating successive cooling-hole configurations. Following completion of the design refinement, the final combustor geometry was analysed using Large Eddy Simulation (LES) to investigate the transient combustion behaviour of both hydrogen and Jet-A fuels. The RANS simulations were used exclusively to compare different cooling-hole configurations under identical modelling assumptions, while the LESs were used solely to compare hydrogen and Jet-A combustion within the final combustor geometry [42]. No direct quantitative comparison is made between the RANS and LES results.

2.6. Boundary Conditions

Mass-flow-rate inlet boundary conditions were specified for both the air and hydrogen inlets, with a turbulence intensity of 5% applied at each inlet. A pressure outlet boundary condition was prescribed at the combustor exit, also with a turbulence intensity of 5%.

Pressure–velocity coupling was achieved using the coupled solver, while all governing equations were discretized using a second-order upwind scheme. Convergence criteria of 10^{-3} were applied to the continuity, momentum, mixture fraction, and mixture-fraction variance equations, whereas the energy equation was converged to 10^{-6}. Table 8 shows boundary conditions values.

Table 8. Boundary Conditions.

Parameter	Value	Unit
Air Inlet Temperature	800	K
Air Inlet Absolute Pressure	3.4	MPa
Air Inlet Mass Flow Rate	5.5	kg/s
Fuel Inlet Temperature	300	K
Fuel Inlet Absolute Pressure	3.5	MPa
Fuel Inlet Mass Flow Rate	0.04	kg/s
Fuel-to-Air Ratio	0.0073	-
Outlet Absolute Pressure	3.2	MPa

The combustor walls were treated as adiabatic no-slip walls throughout the simulations. Consequently, the temperatures reported adjacent to the liner correspond to the near-wall gas temperature rather than the liner metal temperature. The present study focuses on the influence of cooling-hole configuration on the combustor flow and thermal fields, and therefore conjugate heat transfer and structural analyses were not considered.

2.7. Mesh and Mesh Sensitivity

For mesh generation, the tetrahedral method was used with a sphere of influence at the swirler area to improve mesh quality as shown in Figure 2. Table 9 shows the mesh sensitivity study; the mesh sensitivity study was performed by progressively refining the computational mesh and monitoring the mass-flow-averaged outlet temperature.

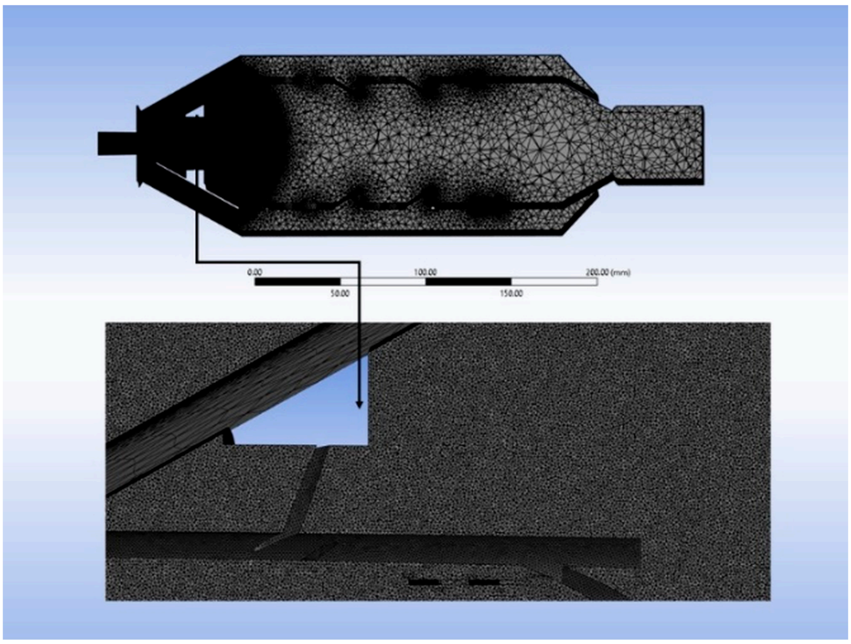

Figure 2. Mesh Used in the Simulation, with a Zoomed-In View of the Refined Mesh in the Swirler and Fuel Diffusion Areas.

Table 9. Mesh Sensitivity Study.

Global Element Size (mm)	Number of Elements	Outlet Temperature (K)
20	1,747,707	1476.58
15	2,212,639	1501.53
10	3,108,716	1510.00
5	9,886,173	1510.28
3	11,018,156	1511.35
1	43,498,273	1513.56

The predicted outlet temperature increased with mesh refinement and showed only a small variation among the three finest meshes, ranging from 1510.28 K for the 5 mm mesh to 1513.56 K for the 1 mm mesh, corresponding to a difference of approximately 3.3 K (0.2%). This small variation indicates that the predicted outlet temperature is relatively insensitive to further mesh refinement over this range. The 5 mm mesh, consisting of approximately 9.89 million elements, was therefore selected for all subsequent steady RANS simulations as it provided a suitable balance between computational cost and solution accuracy during the iterative combustor design process.

3. Results and Discussion

As no experimental data are available for the hydrogen-fuelled annular combustor investigated in this study, the numerical predictions are assessed through comparison with published computational data and through internally consistent design comparisons.

The study employs three complementary comparisons. First, the numerical methodology was assessed against the computational study of Domingues et al. (2022) [27], which represents one of the closest available investigations of hydrogen combustion in a CFM56-class combustor. To enable a direct comparison, the operating conditions reported by Domingues et al. were applied to the present combustor geometry, and the resulting combustor exit temperature, and NO mass fraction were compared with the published results. As the combustor geometries are different, this comparison provides a consistency check of the numerical methodology rather than a direct experimental validation.

Second, the influence of cooling-hole configuration was evaluated by comparing all design iterations under identical modelling conditions. Each configuration was simulated using the same computational domain, mesh strategy, boundary conditions, combustion model, and hydrogen fuel. Consequently, the differences in temperature distribution, fuel-to-air ratio, pressure loss, and NO emissions reported in Sections 3.2–3.5 are attributable solely to the modifications in cooling-hole geometry and cooling-air distribution.

Finally, Large Eddy Simulation (LES) was performed on the final combustor configuration using both hydrogen and Jet-A fuels. This comparison was undertaken using identical combustor geometry and operating conditions to examine the influence of fuel properties on the transient combustion behaviour and emission characteristics.

The comparison with Domingues et al. [27] demonstrated good agreement in combustor exit temperature under identical operating conditions. When the GasTurb-derived operating conditions adopted in the present study were applied, the predicted combustor exit temperature differed by 5.2%, reflecting the higher inlet pressure and temperature associated with the selected design condition. This comparison is intended to demonstrate the consistency of the numerical methodology under different operating conditions rather than to provide experimental validation.

3.1. Temperature Profile

The results demonstrate critical thermal and combustion characteristics of the redesigned combustor. The temperature profile, as illustrated in Figure 3, indicates a favorable airflow distribution, with a gradual reduction in temperature from the primary zone to the outlet.

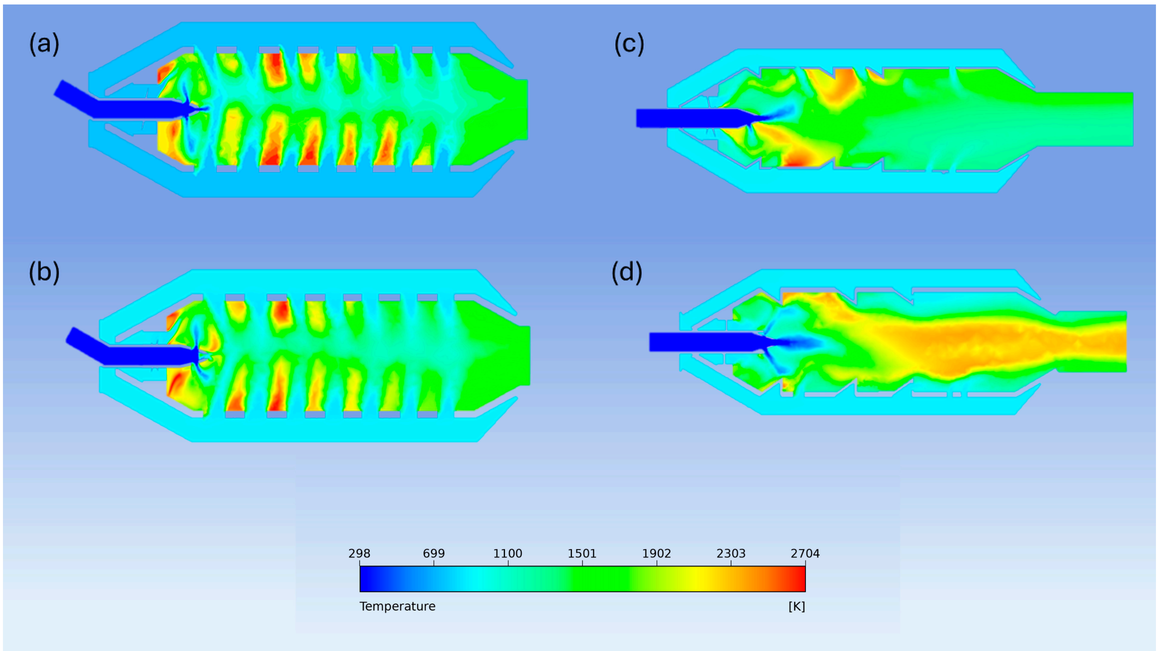

Figure 3. Temperature Distribution in the Combustor, Showing Mean Temperature Fields from Steady-State RANS Simulation Outputs for (**a**) Benchmark Conditions, (**b**) GasTurb 14 Conditions, (**c**) Overcooling, And (**d**) Final Approach.

All contour plots presented in Figures 3–7 were extracted from the mid-plane of the periodic sector, corresponding to the plane passing through the swirler axis and fuel injector. The same section plane was used for every configuration investigated to ensure direct comparison between the benchmark, intermediate, and final cooling layouts. This plane was selected because it captures the principal flow features within the combustor, including the fuel injection region, flame structure, and central recirculation zone.

It should be noted that a single two-dimensional section cannot represent the complete three-dimensional thermal field. Consequently, local temperature variations occurring away from the mid-plane are not fully captured in the contour plots. The temperatures shown in Figures 3–7 therefore represent the thermal behaviour on the selected mid-plane, while the overall combustor performance is evaluated using mass-flow-averaged quantities at the combustor outlet.

The axial temperature profiles presented in Figure 4 illustrate the evolution of the gas temperature through the primary, secondary, and dilution zones, whereas the local temperature contours provide information on the spatial distribution of high-temperature regions within the combustor. Together, these results are used to assess the effectiveness of the different cooling-hole configurations.

Figure 4 illustrates the temperature distribution through the primary, secondary, and dilution zones for the final combustor configuration. The baseline configuration exhibited localised high-temperature regions adjacent to the cooling holes, resulting in increased thermal loading on the combustor liner. Following the redesign of the cooling-hole arrangement, a more uniform temperature distribution was achieved while maintaining the target combustor exit temperature of 1500 K.

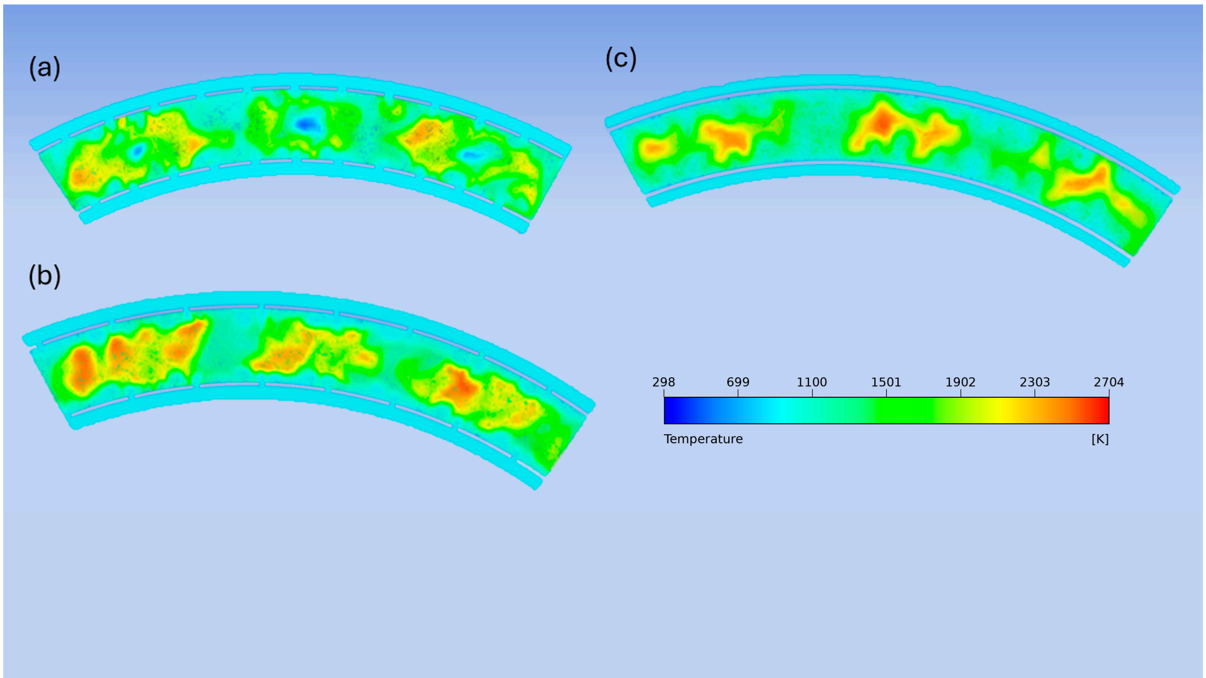

Figure 4. Temperature Distribution in the Combustor, Showing Mean Temperature Fields from Steady-State RANS Simulation Outputs for (**a**) Primary Zone, (**b**) Secondary Zone, And (**c**) Dilution Zone (Final Approach).

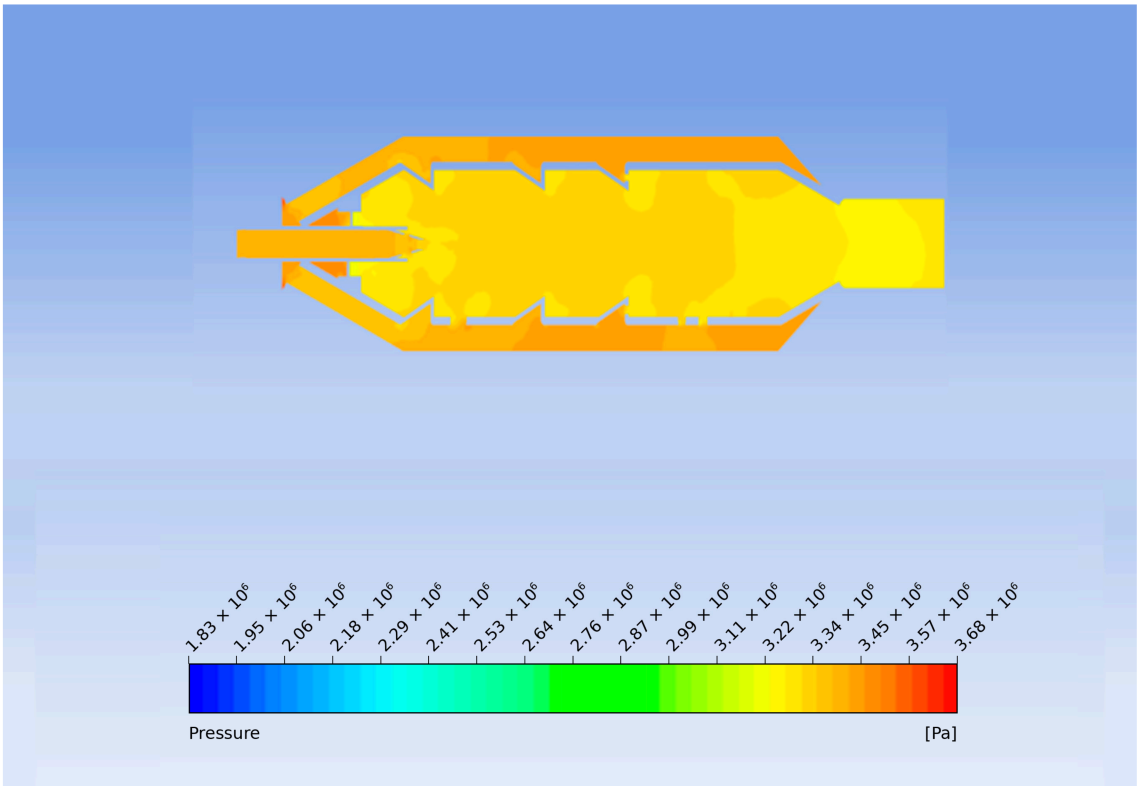

Figure 5. Pressure Distribution Profile in the Combustor, Showing Results from Steady-State RANS Simulation Outputs in the Final Approach.

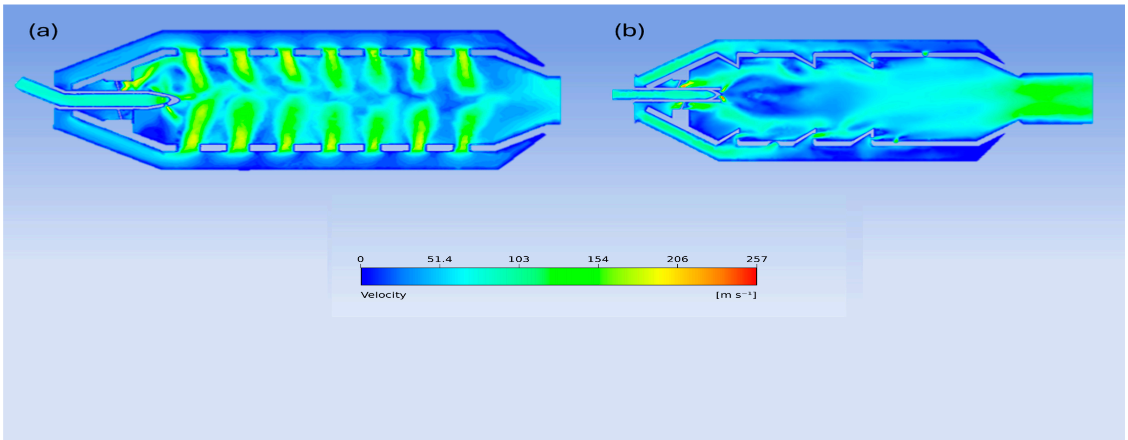

Figure 6. Velocity Profile: (**a**) Initial Approach; (**b**) Final Approach with Cooling Holes.

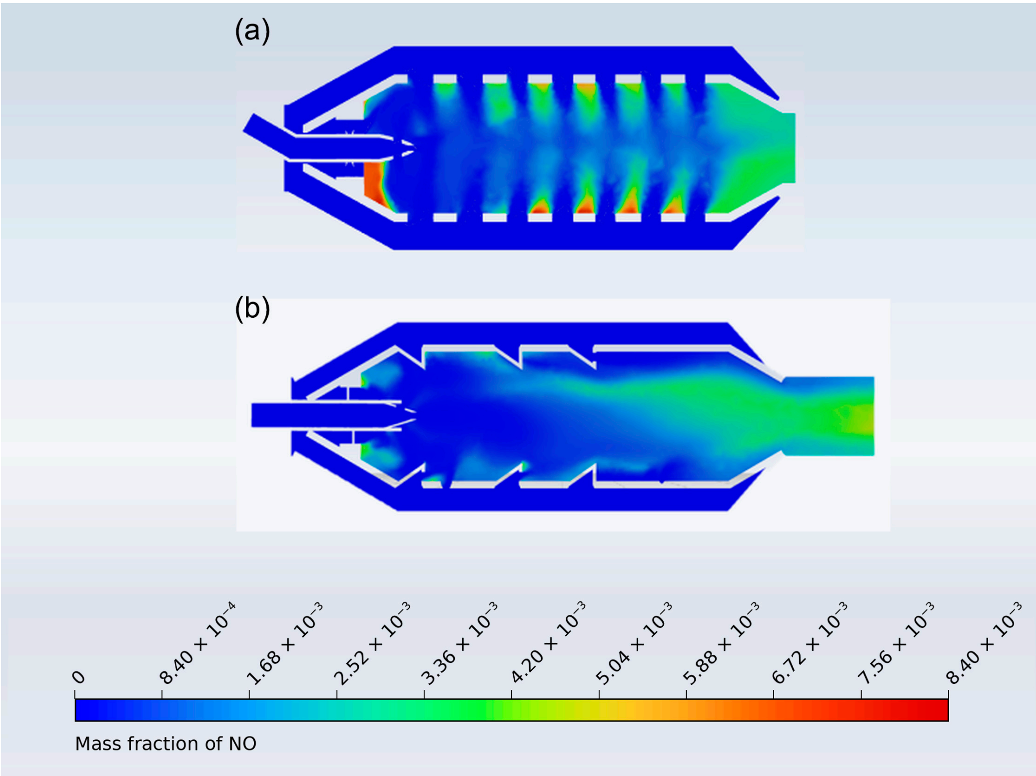

Figure 7. Mass Fraction of No Emissions in: (**a**) Initial Conditions, (**b**) Final Conditions.

The hydrogen fuel-to-air ratio required to achieve the target exit temperature decreased from 0.009 in the initial configuration to 0.0073 in the final configuration, representing a reduction of approximately 18.9%. This improvement is attributed to the redesigned cooling-hole configuration, which enhanced the distribution of cooling air throughout the combustor while maintaining the same operating conditions, computational domain, numerical models, and hydrogen fuel.

The benchmark configuration employed a limited number of relatively large cooling holes concentrated within the primary and secondary zones. This arrangement promoted excessive local cooling of the primary combustion region, reducing the combustion temperature and requiring a higher fuel flow to achieve the desired combustor exit temperature. In contrast, the final design utilised a larger number of smaller cooling holes inclined at ±45°, producing a more uniform cooling-air distribution and improved mixing without excessive quenching of the primary flame. As a result, the target exit temperature was achieved with a lower hydrogen fuel flow, demonstrating improved combustor thermal performance.

For comparison, the operating conditions reported by Domingues et al. [27] were also applied to the present combustor geometry. Under these conditions, the predicted combustor exit temperature showed a deviation of 5.2%, indicating good agreement with the published numerical results despite differences in combustor geometry.

The inlet temperature played a pivotal role in fuel efficiency achievement and in reducing thermal NO_x emissions due to the high flammability of hydrogen. The implementation of a new cooling-hole design addressed these thermal anomalies effectively. The redesigned cooling configuration successfully reduced temperature spikes in critical areas by improving airflow distribution and localized cooling. This not only prolongs the combustion chamber's life by mitigating thermal fatigue but also contributes to a reduction in NO_x emissions, as high temperatures are a significant driver of NO_x formation. The stable outlet temperature of 1500 K in the redesigned configuration verifies the combustor's capability to meet thrust output requirements without compromising operational efficiency. Further analysis revealed an important characteristic of hydrogen combustion; as noted by Domingues et al. (2022) [27], the flame was observed to anchor closer to the swirler outlet when burning hydrogen compared to Jet A fuel, attributed to the higher flame speed of hydrogen. This phenomenon highlights the need for precise design adjustments when integrating hydrogen as a fuel source. These results showcase the improved combustor design as both efficient and environmentally sustainable. In the iterative design process shown in Figure 3, the benchmark cooling hole configuration led to overcooling, resulting in an outlet temperature of 1430 K, even though the fuel-to-air ratio was maintained at 0.009. To improve performance, a new approach was tested, where smaller hole diameters with a greater number of holes were employed in respective zones, inspired by the configuration outlined in a US patent [35]. This adjustment yielded better fuel efficiency while maintaining the same fuel-to-air ratio. However, the issue of wall cooling remained unresolved. Different strategies were then tested, such as increasing the diameter of the cooling holes in the hotter regions, but this approach only shifted the hot spot location without resolving the thermal anomalies. Further exploration led to the implementation of zone-specific cooling holes placed at varying distances, lengths, and angles to optimize temperature distribution. Ultimately, the most effective design featured holes in the primary and secondary zones arranged at a 45-degree angle between the first and second lines. In the dilution zone, a hole pattern with a 45-degree and negative 45-degree orientation was implemented. This arrangement allowed for cooling from all sides, improving the overall aerothermal design. Additionally, reducing hole diameter while increasing the number of holes helped to enhance combustion efficiency while addressing the wall cooling issue more effectively. These refinements significantly contributed to the overall improvement in both thermal management and fuel efficiency, ensuring a more balanced and sustainable combustor design.

3.2. Pressure Distribution

Figure 5 illustrates the total pressure profile within the combustion chamber. The combustor was initially designed to achieve a 6% pressure drop, and the results confirm that this target was successfully met, ensuring stable operation. Although the design incorporates a higher number of holes, which could potentially increase pressure losses, the use of hydrogen as a fuel mitigated this effect. Unlike jet-A fuel, hydrogen combustion generates higher pressure, and the optimized hole configuration, with a slightly higher coefficient of discharge compared to conventional annular combustors, contributed to achieving a favorable temperature profile. This design not only maintained the required pressure but also preserved the structural integrity and lifecycle of the combustor. Most of the pressure drop occurred in the primary and secondary zones, largely due to the coefficient of discharge in these regions. Nevertheless, the total pressure loss remained well within acceptable limits. The outlet pressure, recorded as 3.2 MPa, closely aligned with the combustor's design specifications and matched the predictions obtained through GasTurb version 14 software. This consistency underscores the combustor's reliability and its suitability for integration into a turbofan engine.

The pressure loss across the combustor was maintained at approximately **6%**, consistent with the design requirement adopted in this study. While the inlet total pressure and outlet static pressure were prescribed as boundary conditions, the CFD simulations predict the internal pressure distribution throughout the combustor, including the pressure losses across the diffuser, swirler, annulus, and individual cooling-hole rows. The results indicate that the redesigned cooling-hole configuration provides the intended airflow distribution while satisfying the target pressure-loss requirement. As expected, the largest pressure losses occur across the primary and secondary cooling-hole rows owing to their restricted effective flow area.

The objective of the present study was to improve combustor cooling performance while maintaining a conventional combustor pressure loss. Further reductions in pressure loss could potentially improve overall engine efficiency; however, achieving comparable cooling effectiveness at lower pressure losses would require additional optimisation of the cooling-hole configuration and is recommended as future work.

Even though the pressure is maintained in this design, hydrogen combustion in annular combustors is susceptible to thermoacoustic instabilities due to its high reactivity, fast flame speed, and low ignition energy. These instabilities, often occurring in azimuthal modes, can lead to undesirable pressure oscillations, increased NO_x emissions, and mechanical fatigue, ultimately affecting combustor performance and durability. This study primarily focused on optimizing cooling performance and NO_x reduction in a hydrogen-powered annular combustor. A detailed investigation into thermoacoustic instabilities, including computational or experimental validation, was beyond the scope of this work but remains an important consideration for future research. Since steady-state simulations were conducted in this study, flashback phenomena were not directly observed, as capturing flashback behavior requires time-resolved unsteady simulations or experimental validation. However, flashback remains a critical challenge in hydrogen combustion, and future work should incorporate unsteady CFD simulations (e.g., LES) or experimental studies to assess flame stabilization, flashback risk, and pressure oscillation behavior under realistic operating conditions. To mitigate potential thermoacoustic instabilities, several design modifications could be considered. Swirler geometry optimization can help control vortex shedding, while fuel staging and injector placement can be adjusted to disrupt resonant pressure modes. The incorporation of passive suppression techniques, such as Helmholtz resonators or acoustic damping liners, may further reduce pressure oscillations. Additionally, flashback prevention can be addressed by optimizing injector placement and increasing axial air velocity to ensure the flame remains stabilized in the desired combustion zone. Furthermore, the possibility of a multistage combustor should be explored, as it could not only reduce thermoacoustic instabilities but also lower NO_x emissions by facilitating better fuel–air mixing and staged combustion control. Future studies should investigate these stability-enhancing strategies through unsteady CFD simulations and experimental validation to ensure safe and stable hydrogen combustion in annular gas turbine combustors.

3.3. Velocity Profile

Figure 6 illustrates the velocity magnitude within the combustion chamber, providing critical insights into airflow behavior. High velocities are evident at the swirler inlet and combustion zones, highlighting areas of intense aerodynamic activity.

Additionally, velocity increases are observed near the holes where air transitions from the liner into various zones. These velocity increases contribute to the pressure drop in the corresponding areas, as shown in Figure 5, and are a result of airflow moving from high-pressure to low-pressure regions. In the initial design, high velocities entering from the primary zone posed a potential risk to flame stability. However, this issue was effectively addressed in the final design through the implementation of optimized cooling holes, ensuring improved stability. Across the chamber, the velocity magnitude varies significantly, ranging from 460 m/s to 1 m/s, with the outlet velocity measured at 116.88 m/s. This variation underscores the dynamic nature of the airflow and its critical impact on the overall performance and stability of the combustion chamber.

3.4. NO_x Emissions

Reducing emissions is a critical objective in this study, as demonstrated in Figure 7 showcasing the mass fraction of NO emissions. In the present study, the extended Zeldovich mechanism was employed to model the formation of thermal NO. The key reactions governing this mechanism are outlined in Equations (4)–(7):

$$O_2 \rightleftharpoons 2O \tag{8}$$

$$N_2 + O \rightleftharpoons NO + N \tag{9}$$

$$N + O_2 \rightleftharpoons NO + O \tag{10}$$

$$N + OH \rightleftharpoons NO + H \tag{11}$$

These reactions describe the thermal NO formation pathway, which is the dominant mechanism responsible for NO_x production under the high-temperature combustion conditions considered in this study. As expected, the predicted NO distribution is concentrated in regions of elevated temperature, reflecting the strong dependence of thermal NO formation on flame temperature.

Comparison of the final combustor configuration using hydrogen and Jet-A indicates that hydrogen produces a lower exit NO mass fraction and total NO mass flow rate under the same combustor geometry and operating conditions. However, when expressed as the emission index (EI), hydrogen exhibits a higher value because the NO emissions are normalised by the considerably lower fuel mass required to achieve the same thermal output. Consequently, the different emission metrics provide complementary perspectives on NO_x performance and should be interpreted accordingly.

A comparison with the computational study of Domingues et al. (2022) [27] showed similar NO mass-fraction distributions, with the present study predicting a lower exit NO mass fraction of 0.002223.

According to EASA guidelines (n.d.) [43], emissions are evaluated using the emission index (EI), which is calculated as the ratio of pollutant mass to fuel mass. The calculated EI in this study is 306 g/kg, derived as follows:

$$EI = \text{mass of pollutant (g)}/\text{mass of fuel (kg)} = 306\ \text{g/kg} \tag{12}$$

The final combustor configuration reduced the outlet NO mass fraction from 0.003443 in the initial GasTurb-based configuration to 0.002223, representing a substantial reduction in thermal NO formation while maintaining the target combustor exit temperature. Compared with the benchmark study of Domingues et al. (2022) [27,43], which reported an outlet NO mass fraction of approximately 0.003085 under comparable hydrogen operating conditions, the redesigned combustor achieved a further reduction in NO emissions through improvements in the cooling-hole configuration and air distribution.

The calculated emission index was approximately 306 g/kg based on the predicted NO mass flow rate and hydrogen fuel consumption. Although the emission index is widely used to quantify pollutant emissions, its application to comparisons between hydrogen and conventional hydrocarbon fuels should be interpreted with caution. Hydrogen possesses a lower heating value of approximately 120 MJ/kg, compared with approximately 43 MJ/kg for Jet-A, requiring substantially less fuel mass to produce the same thermal energy. Because the emission index is normalised by fuel mass, hydrogen combustion naturally produces higher EI values even when the NO emissions are comparable or lower than those of conventional fuels. Consequently, additional metrics, such as the Energy Emission Index (EEI), may provide a more representative basis for comparing emissions from fuels with significantly different energy densities.

The present study focuses on the relative improvement achieved through combustor redesign under consistent operating conditions rather than direct comparison with certification limits. Accordingly, the reported NO emissions should be interpreted within the context of the adopted combustion model and operating conditions.

3.5. Large Eddy Simulation Analysis

Direct experimental validation of combustor performance at cruise conditions is currently not feasible. Therefore, a comparative Large Eddy Simulation (LES) study was performed using Jet-A fuel as a reference configuration, alongside hydrogen combustion, to evaluate the geometric and aerothermal improvements introduced in the proposed combustor design under a consistent operating framework. Figure 8 presents the time-averaged temperature contours for (a) Jet-A and (b) hydrogen under identical boundary conditions, while Figure 9 shows the corresponding NO mass-fraction distributions, enabling a direct comparison of flame structure and pollutant formation trends.

The final combustor configuration was further evaluated using Large Eddy Simulation (LES) with both hydrogen and Jet-A fuels under identical operating conditions. This comparison provides an assessment of fuel-dependent combustion behaviour using the same combustor geometry.

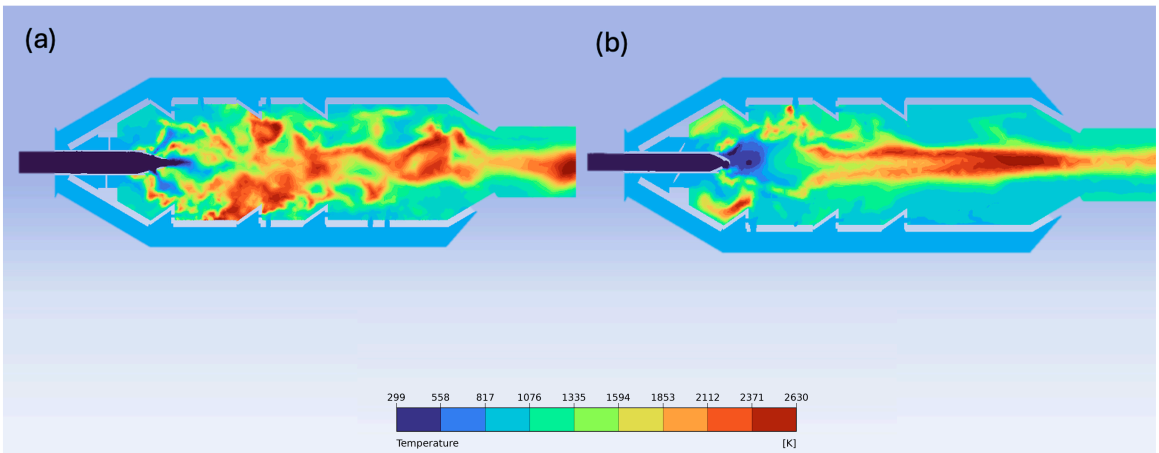

Figure 8. Temperature contours obtained from Large Eddy Simulation for the final optimized combustor configuration: (**a**) Jet-A combustion, (**b**) hydrogen combustion.

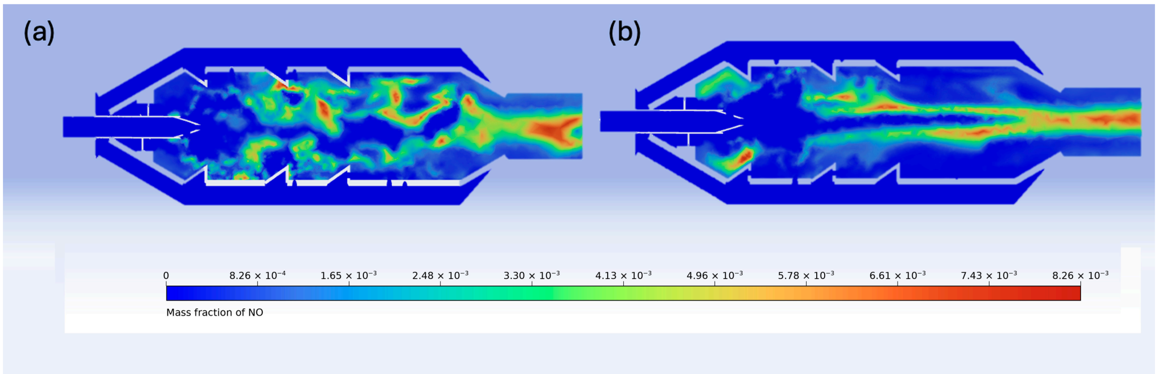

Figure 9. NO mass-fraction contours obtained from Large Eddy Simulation for the final optimized combustor configuration: (**a**) Jet-A combustion, (**b**) hydrogen combustion.

The hydrogen LES case produced a lower outlet NO mass fraction than the corresponding Jet-A case, indicating reduced absolute NO formation under the simulated operating conditions. When expressed as the conventional emission index (EI), however, hydrogen exhibited a higher value because the emission index is normalised by fuel mass. Owing to the substantially higher heating value of hydrogen, less fuel is required to achieve the same thermal output, resulting in a higher EI despite the reduction in absolute NO emissions.

The hydrogen and Jet-A comparisons are presented to illustrate the influence of fuel properties on combustion and emissions, whereas the principal design conclusions of this study are based on the hydrogen-to-hydrogen comparison between the baseline and redesigned combustor configurations.

4. Conclusions

This study presented the aerothermal design and computational assessment of a hydrogen-fuelled annular combustor for a large-bypass turbofan engine. An iterative CFD-guided design approach was used to refine the cooling-hole configuration, with the objective of improving liner cooling while maintaining the target combustor exit temperature and pressure-loss requirements.

The final combustor configuration achieved a target exit temperature of 1500 K with a pressure loss of approximately 5.9%, satisfying the design objective of a 6% pressure drop. Compared with the initial hydrogen combustor configuration under identical operating conditions, the redesigned cooling-hole arrangement reduced the required fuel-to-air ratio from 0.009 to 0.0073, representing an improvement of approximately 18.9%. In addition, the outlet NO mass fraction decreased from 0.003443 to 0.002223, demonstrating that optimisation of the cooling-hole geometry can improve combustor thermal performance while reducing thermal NO formation.

The final cooling configuration employed a larger number of smaller cooling holes, resulting in a more uniform temperature distribution along the combustor liner compared with the benchmark configuration. This reduced localised hot regions and improved cooling effectiveness without increasing the overall combustor pressure loss. The LES investigation further demonstrated the differences in combustion behaviour between hydrogen and Jet-A within the same combustor geometry, providing additional insight into the influence of fuel properties on flame structure and NO formation.

The results presented in this study should be interpreted within the assumptions of the adopted numerical methodology. The simulations were performed using a non-premixed combustion model without thermal radiation or conjugate heat transfer, and no experimental validation was available for the proposed combustor geometry. Consequently, the results are most appropriately considered as a computational design study demonstrating the influence of cooling-hole configuration on combustor aerothermal performance under consistent operating conditions.

Future work should focus on experimental validation of the combustor design, the incorporation of conjugate heat transfer and participating-media radiation models, and the investigation of advanced hydrogen combustion concepts, including lean-premixed, micromix, and staged combustion. Further optimisation of the cooling-hole configuration to reduce pressure loss while maintaining effective liner cooling would also provide a valuable extension of the present work.

Author Contributions: Conceptualization, Y.C. and H.G.D.; methodology, Y.C. and H.G.D.; software, Y.C. and H.S.; validation, Y.C. and H.S.; formal analysis, Y.C.; investigation, Y.C.; resources, H.G.D.; data curation, Y.C.; writing—original draft preparation, Y.C.; writing—review and editing, Y.C., H.S. and H.G.D.; visualization, Y.C.; supervision, H.S. and H.G.D.; project administration, H.G.D. All authors have read and agreed to the published version of the manuscript.

Funding: This research received no external funding.

Data Availability Statement: The data presented in this study are available on request from the corresponding author. The data are not publicly archived because the simulation case files reside on institutional computing resources.

Conflicts of Interest: The authors declare no conflict of interest.

Nomenclature

A_{ref}	Area of Reference
d_h	Hole diameter
d_j	Jet diameter
DZ	Dilution Zone
$\dot{m}_3$	Mass Flow at Combustor Inlet
$\dot{m}_{an}$	Annulus Air Mass Flow Rate
P_3	Pressure At Combustor Inlet
P_4	Pressure At Combustor Outlet
PZ	Primary Zone
q_{ref}	Reference Dynamic Pressure
T_3	Temperature at Combustor Inlet
T_4	Temperature at Combustor Outlet
R	Gas Constant
SZ	Secondary Zone
Tmax	Maximum Temperature
V	Velocity

References

1. Air Transport Action Group. Air Transport Action Group | ATAG. 5 December 2024. Available online: https://www.atag.org/ (accessed on 14 July 2026).
2. Terrenoire, E.; Hauglustaine, D.A.; Gasser, T.; Penanhoat, O. The contribution of carbon dioxide emissions from the aviation sector to future climate change. *Environ. Res. Lett.* **2019**, *14*, 084019. [CrossRef]
3. United Nations. Net Zero Coalition | United Nations. Available online: https://www.un.org/en/climatechange/net-zero-coalition (accessed on 14 July 2026).
4. International Air Transport Association IATA. Net Zero 2050: Sustainable Aviation Fuels. Available online: https://www.iata.org/en/iata-repository/pressroom/fact-sheets/fact-sheet---alternative-fuels/ (accessed on 14 July 2026).
5. Brink, L.; Brown, R.; Mahan, S.; Esqué, A.; Meigs, B.; Riedel, R. *Short-Haul Flying Redefined: The Promise of Regional Air Mobility*; McKinsey & Company: New York, NY, USA, 2023. Available online: https://www.mckinsey.com/industries/aerospace-and-defense/our-insights/short-haul-flying-redefined-the-promise-of-regional-air-mobility (accessed on 14 July 2026).

6. Jaradat, M.; Almashaileh, S.; Bendea, C.; Juaidi, A.; Bendea, G.; Bungau, T. Green Hydrogen in Focus: A Review of Production Technologies, Policy Impact, and Market Developments. *Energies* **2024**, *17*, 3992. [CrossRef]
7. Louli, R.; Giurgea, S.; Salhi, I.; Laghrouche, S.; Djerdir, A. A Critical Review of Green Hydrogen Production by Electrolysis: From Technology and Modeling to Performance and Cost. *Energies* **2026**, *19*, 59. [CrossRef]
8. Abudureyimu, A.; Tuluhong, A.; Chang, Q.; Wang, F.; Luo, B. A Comprehensive Review of Green Hydrogen Technology: Electrolysis Methods, Topologies and Control Strategies, Applications. *Materials* **2025**, *18*, 4826. [CrossRef] [PubMed]
9. Tuluhong, A.; Chang, Q.; Xie, L.; Xu, Z.; Song, T. Current Status of Green Hydrogen Production Technology: A Review. *Sustainability* **2024**, *16*, 9070. [CrossRef]
10. U.S. Department of Energy. Alternative Fuels Data Center: Sustainable Aviation Fuel. Available online: https://afdc.energy.gov/fuels/sustainable-aviation-fuel (accessed on 14 July 2026).
11. Moriarty, K.; Milbrandt, A.; Lewis, J.; Schwab, A. *2017 Bioenergy Industry Status Report*; National Renewable Energy Laboratory: Golden, CO, USA, 2020. [CrossRef] [PubMed]
12. Santos, G. Road transport and CO_2 emissions: What are the challenges? *Transp. Policy* **2017**, *59*, 71–74. [CrossRef]
13. Agarwal, P.; Sun, X.; Gauthier, P.Q.; Sethi, V. Injector Design Space Exploration for an Ultra-Low NOx Hydrogen Micromix Combustion System. In Proceedings of the ASME Turbo Expo 2019: Turbomachinery Technical Conference and Exposition, Volume 3: Coal, Biomass, Hydrogen, and Alternative Fuels; Cycle Innovations; Electric Power; Industrial and Cogeneration; Organic Rankine Cycle Power Systems, Phoenix, AZ, USA, 17–21 June 2019. [CrossRef]
14. Najjar, Y.S.H. Hydrogen safety: The road toward green technology. *Int. J. Hydrogen Energy* **2013**, *38*, 10716–10728. [CrossRef]
15. Muslić, A.; Erden, E.; Balderas-Xicohtencatl, R.; Peter, F.N.; Hornung, M. Fleet-Level Assessment of Hydrogen-Powered Aircraft Using Scenario-Based Modeling. *Aerospace* **2026**, *13*, 517. [CrossRef]
16. Moses, J.K.; Tivfa, T.A.; Qasem, N.A.A.; Alquaity, A.B.S. Combustion Characteristics of Hydrogen, Ammonia, and Their Blends: A Review. *Fuel* **2025**, *388*, 134404. [CrossRef]
17. Jomekian, A.; Naji Alhasnawi, B.; Bazooyar, B.; Nabavi, A.; Varasteh, H. The Effect of Hydrogen Fuel on the Performance and Emissions of 3 kWe Natural Gas Fuelled Microturbine. *Fuel* **2024**, *376*, 132626. [CrossRef]
18. McKinsey & Company. *Hydrogen-Powered Aviation: A Fact-Based Study of Hydrogen Technology, Economics, and Climate Impact by 2050*; Publications Office of the European Union: Luxembourg, 2020; ISBN 978-92-9246-341-0.
19. Thomson, R. *Hydrogen: A Future Fuel for Aviation?* Sederanger 1, 80538; Roland Berger Gmbh: Munich, Germany, 2020.
20. Baroutaji, A.; Wilberforce, T.; Ramadan, M.; Olabi, A.G. Comprehensive investigation on hydrogen and fuel cell technology in the aviation and aerospace sectors. *Renew. Sustain. Energy Rev.* **2019**, *106*, 31–40. [CrossRef]
21. El-Sayed, A.F. Aircraft Propulsion and Gas Turbine Engines. In *Annular Combustion Chamber*; CRC Press: Boca Raton, FL, USA, 2017.
22. Boggia, S.; Jackson, A. Some Unconventional Aero Gas Turbines Using Hydrogen Fuel. In Proceedings of the ASME Turbo Expo 2002: Power for Land, Sea, and Air. Volume 2: Turbo Expo 2002, Parts A and B, Amsterdam, The Netherlands, 3–6 June 2002; pp. 683–690. [CrossRef]
23. Haglind, F.; Singh, R. Design of Aero Gas Turbines Using Hydrogen. *J. Eng. Gas. Turbines Power* **2004**, *128*, 754–764. [CrossRef]
24. Moëll, D.; Lörstad, D.; Bai, X.-S. LES of Hydrogen Enriched Methane/Air Combustion in the SGT-800 Burner at Real Engine Conditions. In Proceedings of the ASME Turbo Expo 2018 Turbomachinery Technical Conference and Exposition, Oslo, Norway, 11–15 June 2018. [CrossRef]
25. Hernandez, C.; McDonell, V.; Delimont, J.; Oskam, G.; Ramotowski, M. Exploring Use of Hydrogen for Extending Operability of a Full-Scale Annular Combustor. In Proceedings of the ASME Turbo Expo 2021 Turbomachinery Technical Conference and Exposition, Virtual, 7–11 June 2021. [CrossRef]
26. Cerutti, M.; Pucci, E.; Romano, C.; Dabiru, V.R. Development of an Hydrogen Fueled Gas Turbine Combustion System From Conceptual Through Full Scale Verification Test. In Proceedings of the ASME Turbo Expo 2023 Turbomachinery Technical Conference and Exposition, Boston, MA, USA, 26–30 June 2023. [CrossRef]
27. Domingues, R.; Brójo, F.; Oliveira, P. CFD Analysis of the Combustion of Hydrogen Fuel on a CFM56-3 Combustor. In Proceedings of the ASME 2022 International Mechanical Engineering Congress and Exposition. Volume 3: Advanced Materials: Design, Processing, Characterization and Applications; Advances in Aerospace Technology, Columbus, OH, USA, 30 October–3 November 2022. [CrossRef]
28. Melconian, J.O.; Modak, A.T. Combustor design. In *Sawyer's Gas Turbine Engineering Handbook Design*; Gas Turbine Publications: Waukesha, WI, USA, 1985; Volume 1, pp. 1–5.
29. Lefebvre, A.H.; Ballal, D.R. *Gas Turbine Combustion: Alternative Fuels and Emissions*, 3rd ed.; CRC Press: Boca Raton, FL, USA, 2010.
30. Mark, C.P.; Selwyn, A. Design and analysis of annular combustion chamber of a low bypass turbofan engine in a jet trainer aircraft. *Propuls. Power Res.* **2016**, *5*, 97–107. [CrossRef]
31. Dharmalingam, S.; Kothari, K.D. Design of a Laboratory Annular Combustor. *Int. J. Aviat. Aeronaut. Aerosp.* **2021**, *8*, 6. [CrossRef]

32. Hodzic, N.; Kazagic, A.; Metovic, S. Influence of over fire air system on NOx emissions: An experimental case study. *Therm. Sci.* **2018**, *23*, 2037–2045. [CrossRef]
33. Fear, J.S.; Lewis Research Center. *Performance of An Annular Combustor Designed for A Low-Cost Turbojet Engine*; National Aeronautics and Space Administration: Washington, DC, USA, 1973. Available online: https://ntrs.nasa.gov/api/citations/19730020186/downloads/19730020186.pdf (accessed on 14 July 2026).
34. Darabkhani, H.G.; Varasteh, H.; Bazooyar, B. *Carbon Capture Technologies for Gas-Turbine-Based Power Plants, Chapter 5*; Elsevier: Amsterdam, The Netherlands, 2022. [CrossRef]
35. Liu, Y.; Sun, X.; Sethi, V.; Nalianda, D.; Li, Y.-G.; Wang, L. Review of Modern Low Emissions Combustion Technologies for Aero Gas Turbine Engines. *Prog. Aerosp. Sci.* **2017**, *94*, 12–45. [CrossRef]
36. Patel, S.; Noble, D.; Emerson, B.; Lieuwen, T. Back to the Future: Revisiting Nonpremixed Designs for Fuel Flexible (H2/NH3/CH4), Low NOx Combustion. *J. Eng. Gas. Turbines Power* **2025**, *147*, 4068587. [CrossRef]
37. Al-Ajmi, R.; Qazak, A.H.; Sadeq, A.M.; Al-Shaghdari, M.; Ahmed, S.F.; Sleiti, A.K. Numerical Investigation of the Potential of Using Hydrogen as an Alternative Fuel in an Industrial Burner. *Fuel* **2024**, *385*, 134194. [CrossRef]
38. Bazooyar, B.; Darabkhani, H.G. Design and Numerical Analysis of a 3 kWe Flameless Microturbine Combustor for Hydrogen Fuel. *Int. J. Hydrogen Energy* **2019**, *44*, 11134–11144. [CrossRef]
39. Li, J.; Zhao, Z.; Kazakov, A.; Dryer, F.L. An updated comprehensive kinetic model of hydrogen combustion. *Int. J. Chem. Kinet.* **2004**, *36*, 566–575. [CrossRef]
40. Strohle, J.; Myhrvold, T. An evaluation of detailed reaction mechanisms for hydrogen combustion under gas turbine conditions. *Int. J. Hydrogen Energy* **2006**, *32*, 125–135. [CrossRef]
41. Peng, D.-Y.; Robinson, D.B. A New Two-Constant Equation of State. *Ind. Eng. Chem. Fundam.* **1976**, *15*, 59–64. [CrossRef]
42. McManus, L.; Fogell, N.; Liu, K.; Sadasivuni, S.; Beita, J.; Munktell, E. Co-Firing Hydrogen with Natural Gas for 9 MW Siemens Energy Dry Low Emissions Combustor: Part II—Large Eddy Simulations. In Proceedings of the ASME Turbo Expo 2025: Turbomachinery Technical Conference and Exposition, Memphis, TN, USA, 16–20 June 2025. [CrossRef]
43. European Union Aviation Safety Agency (EASA). ICAO Aircraft Engine Emissions Databank | EASA. EASA. Available online: https://www.easa.europa.eu/en/domains/environment/icao-aircraft-engine-emissions-databank (accessed on 14 July 2026).